Additive Manufacturing 72 (2023) 103623

Contents lists available at ScienceDirect

Additive Manufacturing

journal homepage: www.elsevier.com/locate/addma

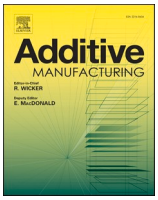

Crack reduction in Inconel 939 with Si addition processed by laser powder bed fusion additive manufacturing

Bin Zhang [a,*,1], Huan Ding [a,1], Andrew C. Meng [b], Saber Nemati [a], Shengming Guo [a], W.J. Meng [a]

[a] Department of Mechanical and Industrial Engineering, Louisiana State University, Baton Rouge, LA 70803, USA
[b] Department of Physics and Astronomy, University of Missouri, Columbia, MO 65211, USA

ARTICLE INFO

Keywords:
Laser powder bed fusion
Ni-based superalloy
Inconel 939
Cracking mechanisms
Si addition

ABSTRACT

Inconel 939 (IN939) suffers from cracking in the laser powder bed fusion based additive manufacturing (LPBF-AM) process. Previous studies attempted to minimize the crack density by reducing the Si content. In contrast, this paper demonstrates that Si addition can substantially lower the crack density in LPBF-AM IN939 alloy parts. Si addition into IN939 shows a moderate impact on the crystallographic orientation and grain size of LPBF-AM parts, and promotes the formation of precipitates. Mechanical tests show that Si addition increases tensile strength and indentation hardness but decreases ductility. This work suggests that the dominant cracking mode in LPBF-AM IN939 alloy parts is solidification cracking, the suppression of which by Si addition can be qualitatively rationalized using Clyne's model and Kou's model. The present findings provide a different perspective on designing defect-free LPBF-AM Ni-based superalloy parts with balanced mechanical properties, one which can be extended to other alloy systems.

1. Introduction

Over the last two decades, laser powder bed fusion based additive manufacturing (LPBF-AM) has been widely used to fabricate various metallic parts with excellent mechanical properties [1–4]. LPBF-AM is characterized by high design flexibility, short lead time, and low waste, and is attractive for manufacturing materials with high strength and poor machinability, including Ni-based superalloys, which are difficult to process using conventional subtractive machining techniques [5]. Extensive studies have been reported on the microstructural evolution and mechanical performance of additively manufactured Ni-based superalloy parts, over 80% of which focus on Inconel 718 (IN718) and Inconel 625 (IN625) alloys due to their relatively good weldability [6]. However, some non-weldable Ni-based superalloys, such as CM247LC [7] and Inconel 939 (IN939) alloy [8], tend to contain a high density of cracks after LPBF-AM processing. Therefore, the fabrication of crack-free Ni-based superalloys with poor weldability has continued to be a research focus.

IN939 presents high strength/toughness, high creep/oxidation/corrosion resistance, and microstructure stability up to 850 °C, and is well suited for aerospace and energy sector applications [9]. IN939 is mainly strengthened by the γ'-Ni_3(Al, Ti) phase and its poor weldability stems from the high total content of Al and Ti [10]. The LPBF-AM process, combining a high energy density laser source, high scanning speed, and high cooling rate, tends to result in high residual stresses, which exacerbates the occurrence of cracking in IN939 specimens [8]. However, only limited data have been reported on the cracking mechanisms of IN939 during LPBF-AM processing. Kanagarajah et al. [11] investigated the microstructure and mechanical properties of LPBF-AM IN939, mainly focusing on the heat treatment effect. However, the presence of micro-cracks in as-built IN939 specimens was not characterized. Marchese et al. [8] studied the influence of the process parameters on the densification and microstructure of LPBF-AM IN939. They concluded that printing parameter optimization could reduce the porosity and crack density, but crack-free IN939 was unachievable. Tang et al. [12] characterized the cracking behaviors in LPBF-AM IN939 and CM247LC specimens. The observed cracks were categorized into three types: solidification cracking, liquation cracking, and solid-state cracking. Both solidification cracking and solid-state cracking were identified in IN939 specimens based on detailed fractography analysis.

Solidification cracking, also known as hot tearing, occurs at the last stage of solidification where the feeding of liquid to counteract

* Corresponding author.
E-mail address: bzhan15@lsu.edu (B. Zhang).
[1] Authors who have contributed equally to this article

https://doi.org/10.1016/j.addma.2023.103623
Received 13 December 2022; Received in revised form 10 May 2023; Accepted 21 May 2023
Available online 23 May 2023

solidification shrinkage is hindered and the thin liquid film in the semi-solid region is teared due to the tensile thermal deformation [13]. These thin liquid films locate at the interdendritic regions, which form grain boundaries after complete solidification [14]. Studies have reported on the effect of minor alloying elements in Ni-based superalloys on solidification cracking during LPBF-AM processing. Tomus et al. [15] reported the LPBF-AM Hastelloy X alloy with reduced Mn+Si content contained much lower porosity and crack density. Engeli et al. [16] also reported that the Si element in IN738LC alloy needed to be restricted because Si enrichment at grain boundaries formed detrimental phases and increased the cracking susceptibility. Cloots et al. [17] attributed the solidification cracking observed in LPBF-AM IN738LC to Zr enrichment at grain boundaries. They hypothesized that Zr enrichment leads to an increase in the critical solidification temperature range (CSTR) at grain boundaries, making it more susceptible to solidification cracking. However, Hariharan et al. [18] disagreed with the above hypothesis. Instead, they proposed that the influence of Zr and Si on grain boundary energies and solid-liquid interface energies was responsible for solidification cracking.

Though the mechanisms of how the minor solute elements influence the solidification cracking of LPBF-AM Ni-based superalloys remain contentious, various research works in the literature [15–18] consistently conclude that an increase in Si content increases the cracking susceptibility. Nevertheless, recent studies report that crack density in LPBF-AM Al alloys has been significantly reduced by adding Si [19–21]. This motivates us to investigate whether Si addition also helps to fabricate crack-free LPBF-AM Ni-based superalloy parts with balanced mechanical properties. In this work, we report, for the first time to the best of our knowledge, that Si addition can substantially lower the crack density in LPBF-AM IN939 alloy parts. Microstructure and mechanical properties of LPBF-AM IN939 with and without Si addition are investigated. The associated cracking mechanisms are also discussed.

2. Calculation and experimentation procedures

2.1. Crack susceptibility coefficient (CSC) calculation

CSC describes the crack tendency of materials. To assess the effect of Si addition on the crack susceptibility in the IN939 system and guide the subsequent fabrication of IN939 specimens with varying Si content, CSC was assessed using the Calculation of Phase Diagrams (CALPHAD) software Thermo-Calc with the Clyne's model[22]. The TCNI8: Ni-alloy v 8.2 database was adopted. In Clyne's solidification cracking criteria, the CSC is defined as:

$$CSC = \frac{t_V}{t_R} \tag{1}$$

where t_V is the solidification time during which the alloy is vulnerable to cracking, and generally refers to the time spent as the solid volume fraction (f_S) increases from 0.9 to 0.99; t_R is the available time for the alloy to relieve the accumulated stress, and is defined as the time spent in the f_S range of 0.4–0.9. Fig. 1 plots the calculated CSC values as a function of added Si content (wt%). The CSC value increases significantly as the Si content reaches ~0.5 wt%. As the Si content increases further to 1.5 wt%, the CSC value drops sharply from ~3.2 to ~1.3, and then varies in the range of ~1.3 to ~1.0. This indicates a higher Si content, e.g., over 0.8 wt%, would substantially decrease the cracking tendency of IN939 alloy. The CSC value further decreases to ~0.6 at ~3.0 wt% Si, and then begins to increase with higher Si content, as the deleterious effects of Si become prominent. In this work, IN 939 specimens with no Si addition, 1.5 wt% and 3.0 wt% Si addition were fabricated by LPBF-AM. In what follows, these specimens are denoted respectively by pure-IN939, IN939 + 1.5%Si and IN939 + 3.0%Si.

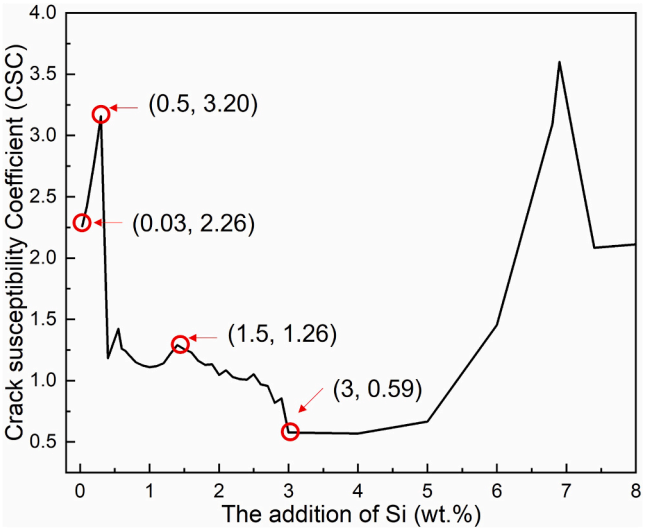

Fig. 1. Calculated crack susceptibility coefficient (CSC) as a function of Si addition.

2.2. Powder mixing and LPBF-AM processing

Commercial spherical gas atomized IN939 powder (Carpenter Additive, USA) and commercial Si particles (Alfa Aesar, USA) are used in this work. Fig. 2(a) shows the surface morphology of the IN939 powder, with its chemical composition listed in Table 1. The powder size distribution is single-peaked, as shown in Fig. 2(b), with a peak value of 30.2 μm. The D_{10} and D_{90} values were determined respectively to be 18.9 μm and 45.3 μm using a Mastersizer 3000 (Malvern AERO S, dry powder dispersion mode). Fig. 2(c) displays the flake-shaped silicon powder with a purity of > 99.5%. The average Si powder size is measured to be 4.5 μm. Pure IN939 powder and Si powder were mixed in a SPEX 8000 m MIXER for 10 h. Fig. 2(d) shows the morphology of the uniformly mixed IN939 powder with 3.0 wt% Si powder.

LPBF-AM specimens with dimensions of 10 mm × 10 mm × 6 mm (Fig. 3(a)) were fabricated using a custom-built selective laser melting machine under a flowing argon atmosphere. The optimized LPBF-AM processing parameters of layer thickness *t*, laser power *P*, laser scan speed *ν*, and hatch space *h* are selected to be 0.05 mm, 160 W, 100 mm/s, and 0.05 mm, respectively. A simple 'back-and-forth scanning strategy' was used, with no rotation across layers (Fig. 3(a)).

2.3. Mechanical testing

Instrumented nanoindentation hardness measurements were performed on surfaces perpendicular to the build direction of LPBF-AM specimens on a Nanointenter XP system (MTS Systems Corp., Knoxville, TN) with a diamond Berkovich indenter. A force-controlled mode was used at a loading rate of 0.2 mN/sec. Before the indentation measurements, specimen surfaces were mechanically polished successively with SiC papers and polycrystalline diamond suspensions, followed by a 12-hour vibratory polish with 50 nm silica suspension (Pace Technologies GIGA 0900 Vibratory Polisher).

Micro-tensile tests were conducted in-situ an FEI Quanta3D FEG Dual-Beam scanning electron microscope/Ga+ focused ion beam (SEM/FIB) instrument using an instrumented nanomechanical testing system (FemtoTools-NMT04). A displacement-controlled mode was used at a displacement rate of 30 nm/sec, leading to a typical nominal strain rate of 10^{-3}/sec with a typical gauge length of 30 μm. Dogbone-shaped micro tensile specimens were cut using a Xe plasma focused ion beam instrument (PFIB, ThermoFisher Helio G4).

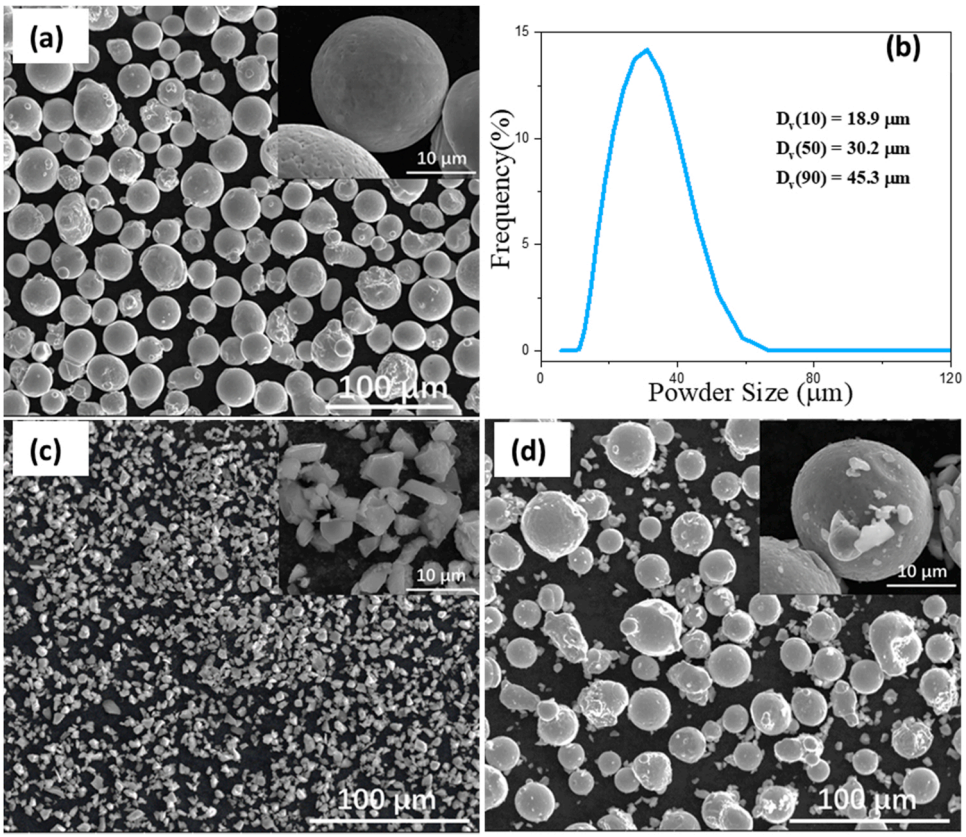

Fig. 2. (a) An SEM image of the commercial IN939 powder; (b) size distribution of the commercial IN939 powder; (c) an SEM image of the commercial pure Si powder; (d) an SEM image of the IN939 + 3.0%Si powder mixture.

Table 1
Elements content of the commercial IN939 powder (wt%).

Ni	Cr	Co	Ti	Al	C	Nb	Ta	W	Si	B	Zr
Balance	15.7	8.1	3.3	3.3	< 0.2	0.9	1.7	2.7	0.03	0.011	0.06

2.4. Materials characterization

The aforementioned mechanical polishing procedure was employed prior to electron backscatter diffraction (EBSD) mapping and metallographic etching. EBSD mapping was performed at 30 kV and 23 nA with an EBSD attachment (EDAX) on the FEI Quanta3D FEG Dual-Beam SEM/FIB system. Raw EBSD data were analyzed with the TSL OIM software. Metallographic etching was conducted using the waterless Kalling's reagent, and a Keyence VH-Z100UR digital microscope was used for optical microscopy (OM) images.

3D visualizations for determining the size and distribution of internal cracks within as-printed specimens were conducted using a ZEISS X-ray micro-computed tomography system (micro-CT, Xradia 620 Versa). Rectangular cylinders with dimensions of ~2 mm × 2 mm × 5 mm were cut out of as-printed pure-IN939 and IN939 + 3.0%Si specimens, and examined with micro-CT at a scan voxel size of 0.7 μm. The software package Avizo was used to process the data.

X-ray diffraction (XRD) examination was performed on a PANalytical Empyrean system with Cu Kα radiation. Symmetric θ/2θ scans were conducted in the angular range of 30–120° 2θ, with a scanning step size of 0.05°. Transmission electron microscopy (TEM) specimens were prepared following a standard Omniprobe lift-out and thinning process [23]. TEM characterization was conducted on a JEOL JEM-F200 Scanning/Transmission Electron Microscope (S/TEM) operated at 200 kV. STEM characterization was conducted on a JEOL NEOARM 30–200 kV S/TEM equipped with dual silicon-drift detector x-ray energy dispersive spectroscopy (EDS) systems with a large solid angle (1.7 sr). STEM-EDS maps were collected using probe size 6 C and a 40 μm condenser aperture (~ 120 pA probe current).

3. Results

3.1. Crack morphology and quantitative assessment

Fig. 3 illustrates the specimen dimensions and the etched cross-sections in the xz-plane (parallel to the build direction, BD) of as-fabricated pure-IN939, IN939 + 1.5%Si, and IN939 + 3.0%Si specimens. Three etched cross-sections were examined in each specimen. The microstructure is dominated by columnar grains aligned approximately along BD, consistent with previous observations [6]. Numerous long cracks are visible in the pure-IN939 specimen, as shown in Fig. 3(b). These cracks locate at grain boundaries and go through a few layers along BD. Only one short crack is observed in the IN939 + 1.5%Si specimen (Fig. 3(b)) and no cracking is observed in the IN939 + 3.0%Si specimen, indicating that the addition of Si has successfully reduced the amount of cracking.

The OM inspection shown in Fig. 3 is further confirmed by quantitative measurements from micro-CT scans. Fig. 4(a) and (b) display the 3D visualizations of internal cracks in the pure-IN939 specimen. The cracks are largely planar, as highlighted by the black arrows in Fig. 4(a).

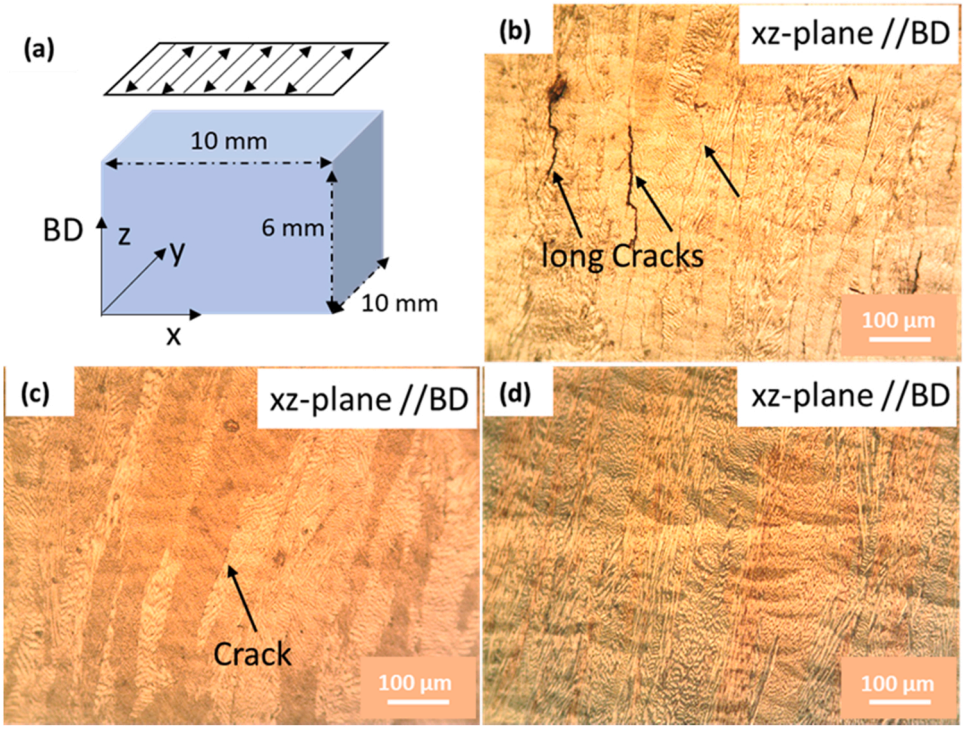

Fig. 3. (a) LPBF-AM specimen dimensions, and a schematic diagram showing the scanning strategy; (b) an OM image of etched pure-IN939 with numerous long cracks; (c) an OM image of etched IN939 + 1.5%Si with reduced cracking; (c) an OM image of etched IN939 + 3.0%Si without cracks in the field of view.

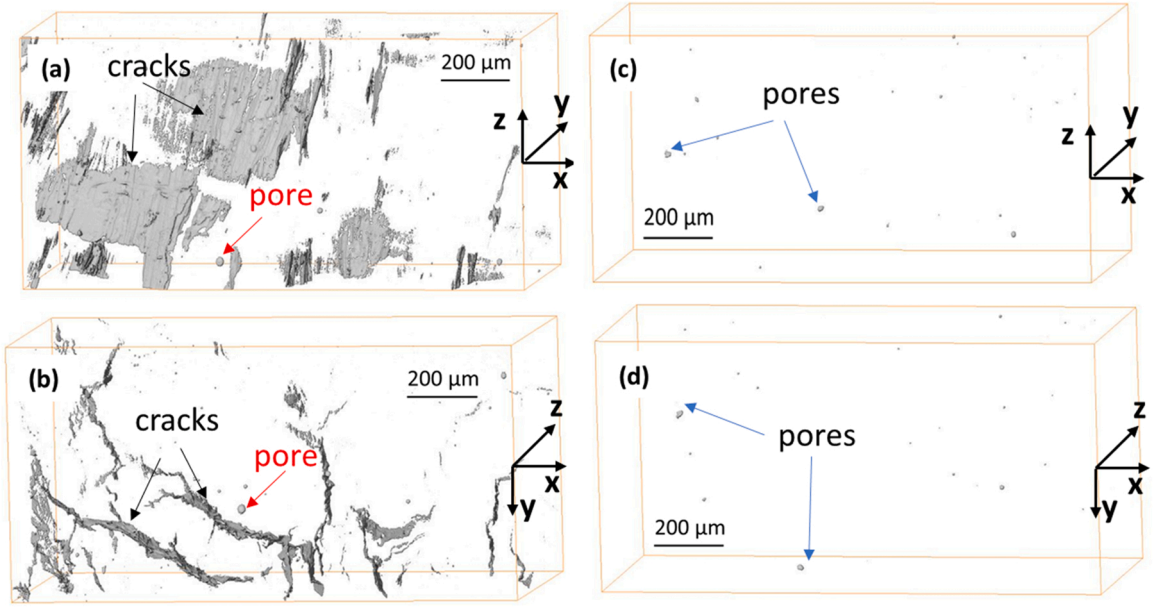

Fig. 4. X-ray micro-CT showing the morphology of cracks: (a/b) Pure IN 939; (c/d) IN939 + 3.0%Si.

They turn into line-like features after rotating along the x-axis by 90°, as highlighted by the black arrows in Fig. 4(b). This indicates that the cracks develop along the z direction (BD). The crack lengths along the z-direction vary from tens of microns to hundreds of microns. Some large pores are also detected, as highlighted by the red arrows in Fig. 4(a) and (b). The volume fraction of cracks and pores is measured to be 1.94×10^{-3}. Fig. 4(c) and (d) display the associated micro-CT scans of the IN939 + 3.0%Si specimen. Some pores are visible (blue arrows), but no cracks are detected. The volume fraction of pores is determined to be 4.49×10^{-5}, two orders of magnitude below the crack/pore volume fraction of the pure-IN939 specimen.

3.2. Microstructure and texture development

Fig. 5 presents the EBSD inverse pole figure (IPF) Z maps and the corresponding pole figure (PF) plots and inverse pole figure (IPF) plots in the xy plane (perpendicular to BD, see Fig. 3(a)) of as-fabricated pure-IN939, IN939 + 1.5%Si, and IN939 + 3.0%Si specimens. For all three specimens, the PFs and IPFs reveal a preferred texture of {100}< 001 >, indicating a single cube texture component [24]. This is typical

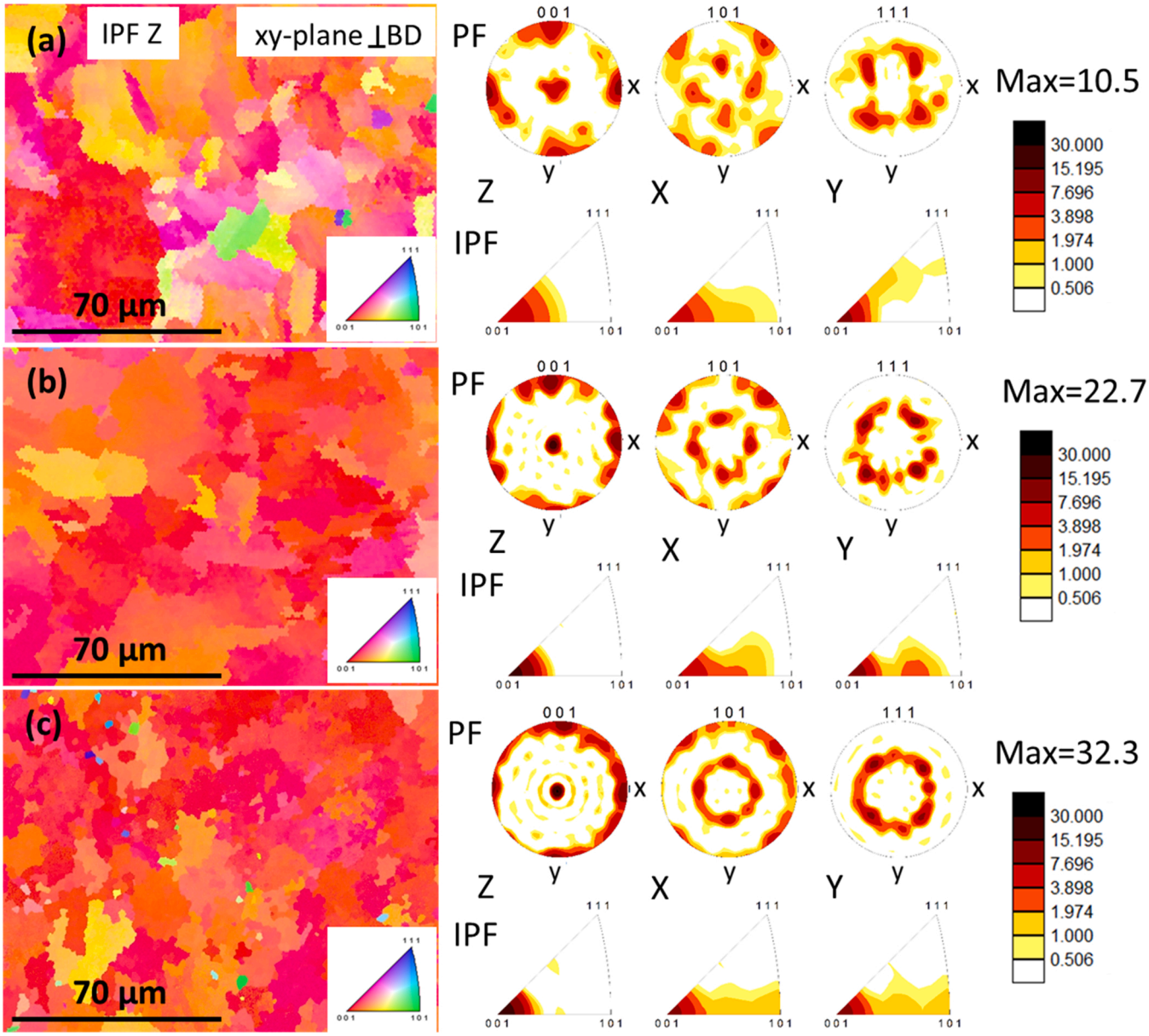

Fig. 5. EBSD IPF Z maps of surfaces perpendicular to the build direction and the corresponding pole figures (PF) and inverse pole figures (IPF) of as-built specimens: (a) pure-IN939; (b) Ni939 + 1.5%Si; (c) Ni939 + 3.0%Si.

for additively manufactured face-centered cubic (FCC) metals due to the directional solidification effect [25]. It is noted that the texture strength increases significantly with increasing Si content, as shown by the maximum texture intensity increasing from 10.5 for pure-IN939 to 32.3 for the IN939 + 3.0%Si specimen. This tendency is also evidenced in the more randomized IPF map color in Fig. 5(a), indicating weaker texture in pure 939.

Fig. 6 presents the EBSD inverse pole figure (IPF) Y maps and the corresponding pole figure (PF) plots and inverse pole figure (IPF) plots in the xz plane (parallel to BD, see Fig. 3(a)) of as-fabricated pure-IN939, IN939 + 1.5%Si, and IN939 + 3.0%Si specimens. The IPF map color distribution changes substantially with varying Si content, indicating the Si addition into IN939 leads to a significant transition in crystallographic orientation. The PFs and IPFs demonstrate clearly that the pure-IN939 specimen still exhibits a preferred cube texture of {100}< 001 > with a maximum texture intensity value of 17.3. However, both IN939 + 1.5%Si and IN939 + 3.0%Si specimens display a preferred goss texture component of {110}< 001 > , and the goss texture strengthens with increasing Si content.

IPFs in Fig. 6 confirm the formation of large columnar grains along BD, as shown in Fig. 3. To evaluate the effect of Si addition on the microstructure, the widths of columnar grains are measured from the point-to-point misorientation angle plots. Fig. 7(a) displays one such plot, obtained along the path indicated by the double arrow *pq* in Fig. 6 (a). Peaks with a misorientation angle greater than 15° are taken to represent grain boundaries. Similarly, Fig. 7(b) and (c) show the corresponding point-to-point misorientation angle plots for IN939 + 1.5% Si and IN939 + 3.0%Si specimens, and Fig. 7(d) plots the average grain width with error bars stemming from at least three line measurements for each specimen. The 3 wt% Si addition reduces the average columnar grain width from 14.8 ± 2.3 μm to 9.7 ± 1.0 μm.

Fig. 8(a) displays the XRD $\theta/2\theta$ scans from raw IN939 powders, and as-printed pure-IN939, IN939 + 1.5%Si, and IN939 + 3.0%Si specimens with their x-y planes being the specimen plane. It is evident that the main phase present in all specimens is the FCC γ NiCr phase. Because the peaks corresponding to the γ′ phase can overlap with the γ peaks, it is

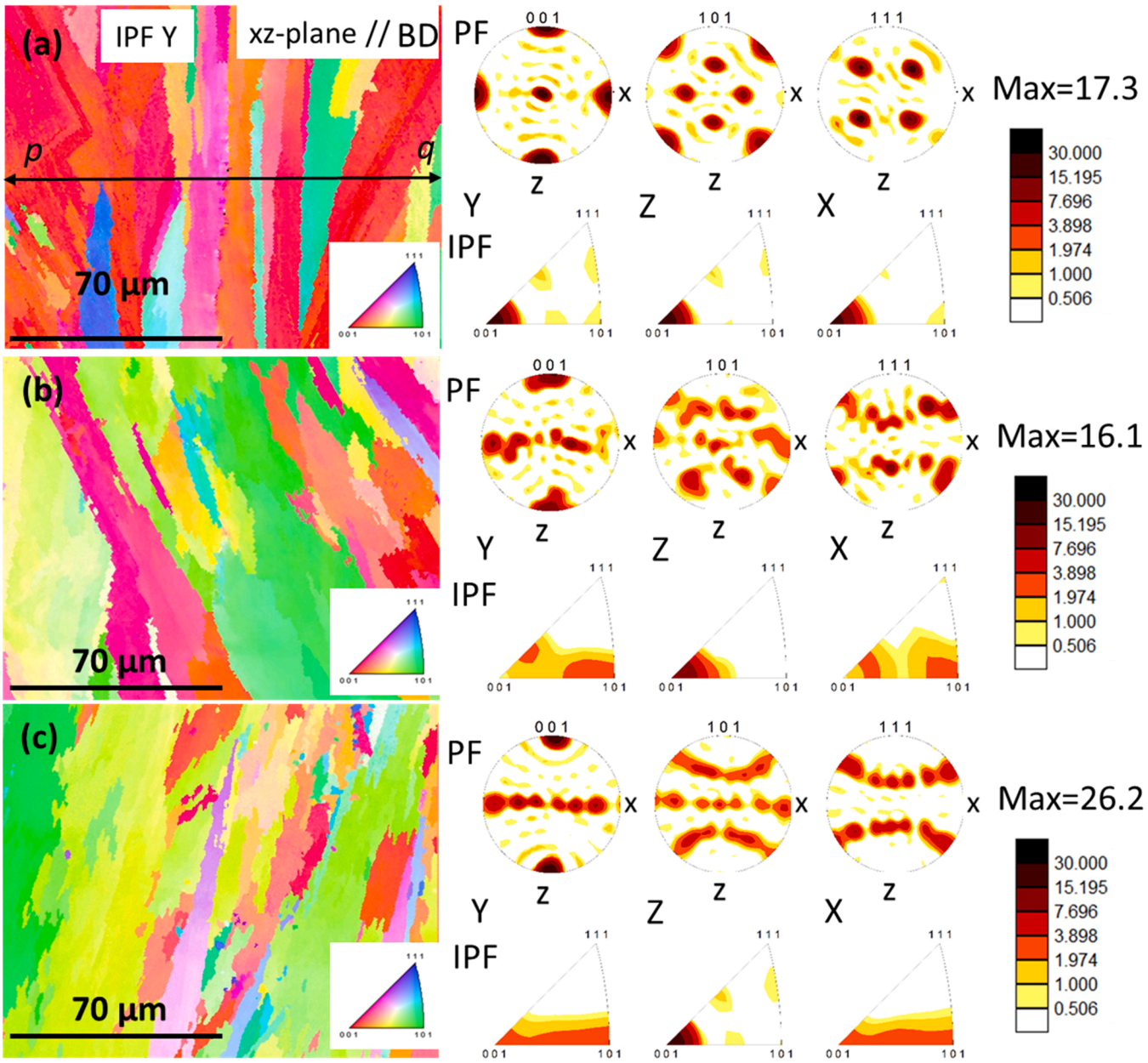

Fig. 6. EBSD IPF Y maps of surfaces parallel to the build direction and the corresponding pole figures (PF) and inverse pole figures (IPF) of as-built specimens: (a) pure-IN939; (b) Ni939 + 1.5%Si; (c) Ni939 + 3.0%Si.

difficult to separate the γ/γ′ phases by peak analysis. Pure-IN939, IN939 + 1.5%Si, and IN939 + 3.0%Si specimens exhibit a high intensity (200) peak, consistent with the conclusion of the EBSD texture analysis. It should be noted that two extra low-intensity peaks were detected from the IN 939 + 3.0%Si specimen, indicating the formation of new phases due to the Si addition. Fig. 8(b) shows the $\theta/2\theta$ scans over a narrower 2θ range of $49^\circ - 53^\circ$. It is evident that (200) diffraction peaks in as-printed specimens shift towards larger angles as compared to that of the as-received IN939 powder, and an increased angle shift accompanies increasing Si addition. Specifically, the 2θ angle of (200) diffraction peaks of pure-IN939, IN939 + 1.5%Si, and IN939 + 3.0%Si specimens are 50.84°, 50.95°, and 51.13°, respectively. The corresponding lattice parameters, calculated using $\lambda = 0.154$ nm (Cu $K\alpha_1$), are respectively 0.3587 nm, 0.3581 nm, and 0.3573 nm. Compared to pure-IN939, the changes in lattice parameter with 1.5 wt% and 3.0 wt% Si addition are − 0.17% and − 0.39%, respectively. This suggests the Si addition could promote the migration of solute atoms away from the γ phase lattice to form precipitates, thus reducing the lattice parameter of the γ matrix. The other point worth considering is that the addition of Si might have changed the melt pool geometries, and hence the residual stress distribution that affected the lattice spacing (via compression or expansion of lattices). The change of melt pool shapes from particle additions has been documented in some publications [26,27].

The formation of precipitates can be confirmed through metallographic etching, as shown in Fig. 9. Fig. 9(a) shows an SEM image of the etch surface parallel to BD (x-z plane) of the pure-IN939 specimen. A higher magnification view of the area highlighted by the red rectangle in Fig. 9(a) is shown in Fig. 9(b). Nanoscale precipitates are shown as bright particles along the interdendritic regions, consistent with previous results [8]. Fig. 9(c) shows an SEM image of the etch surface perpendicular to BD (x-y plane) of the same as-printed pure-IN939 specimen. Cellular structures are visible, and precipitates formed at the cell boundaries as highlighted by the black arrow in Fig. 9(c). Analogous SEM images of etched surfaces of as-printed IN939 + 1.5%Si and

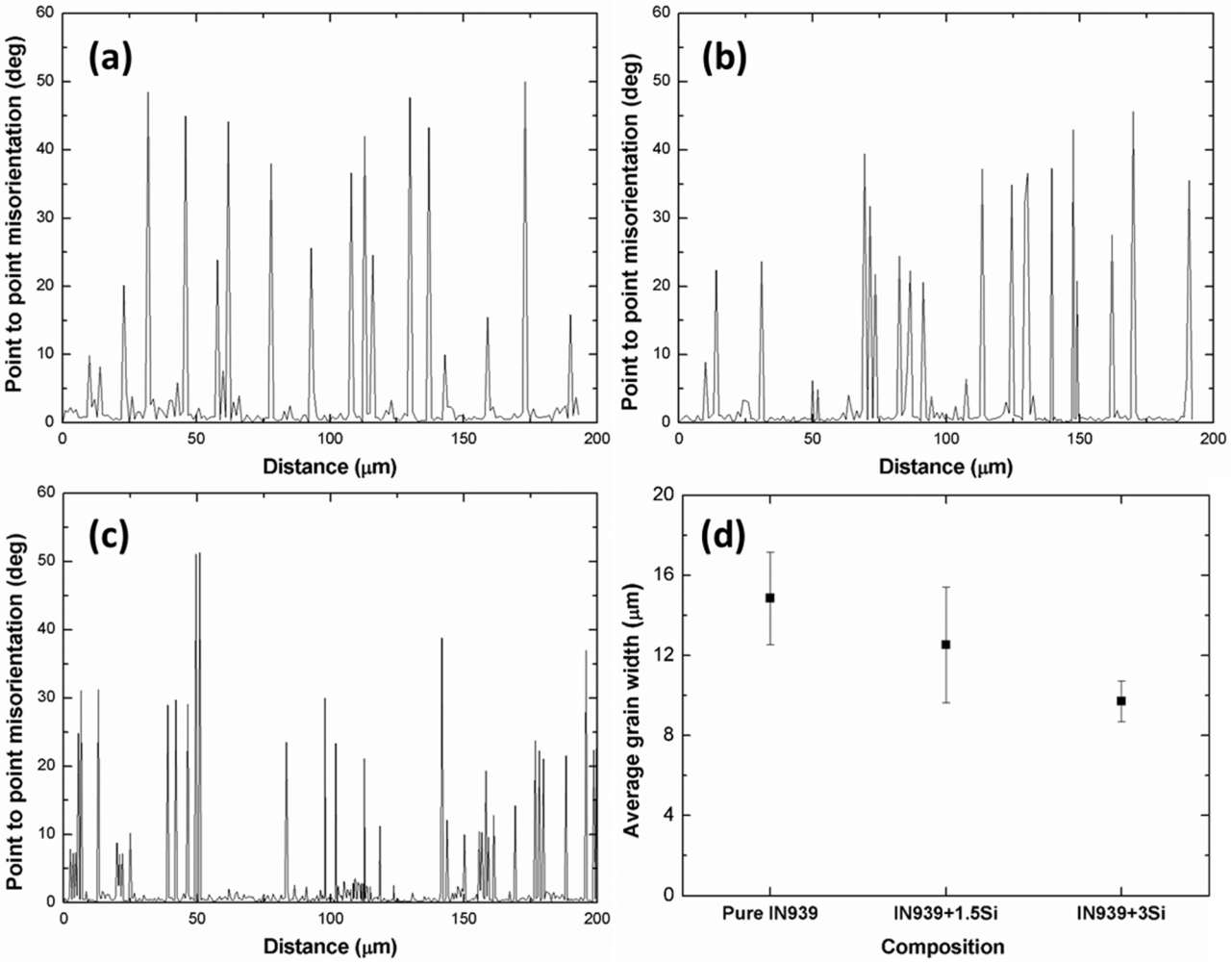

Fig. 7. Point-to-point misorientation angle plots for measuring the average grain width: (a) pure-IN939; (b) IN939 + 1.5%Si; (c) IN939 + 3.0%Si; (d) the average grain width vs. Si addition into IN939.

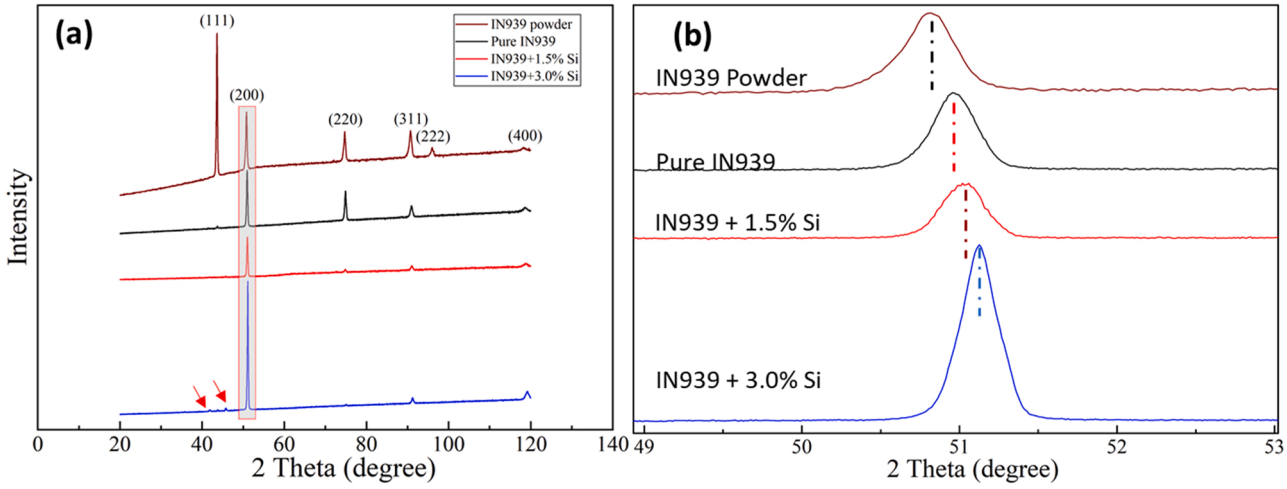

Fig. 8. XRD θ/2θ scans: (a) θ/2θ scans over the 2θ angle range of 20° - 120° from raw IN939 powders, as-built pure-IN939, IN939 + 1.5%Si, and IN939 + 3.0%Si specimens; (b) θ/2θ scans over a narrow 2θ angle range of 49° - 53°. The two red arrows in (a) mark the occurrence of extra diffraction peaks not indexable to the γ/γ' phase.

IN939 + 3.0%Si specimens are shown respectively in Fig. 9(d/e/f) and Fig. 9(g/h/i). It is evident that the degree of the precipitate formation increases with increasing Si addition. Grain boundaries can be recognized, as indicated by black dashed lines in Fig. 9(d/e), roughly along the build direction, and the precipitates exhibit varying morphologies within different grains. As shown more closely in Fig. 9(e),

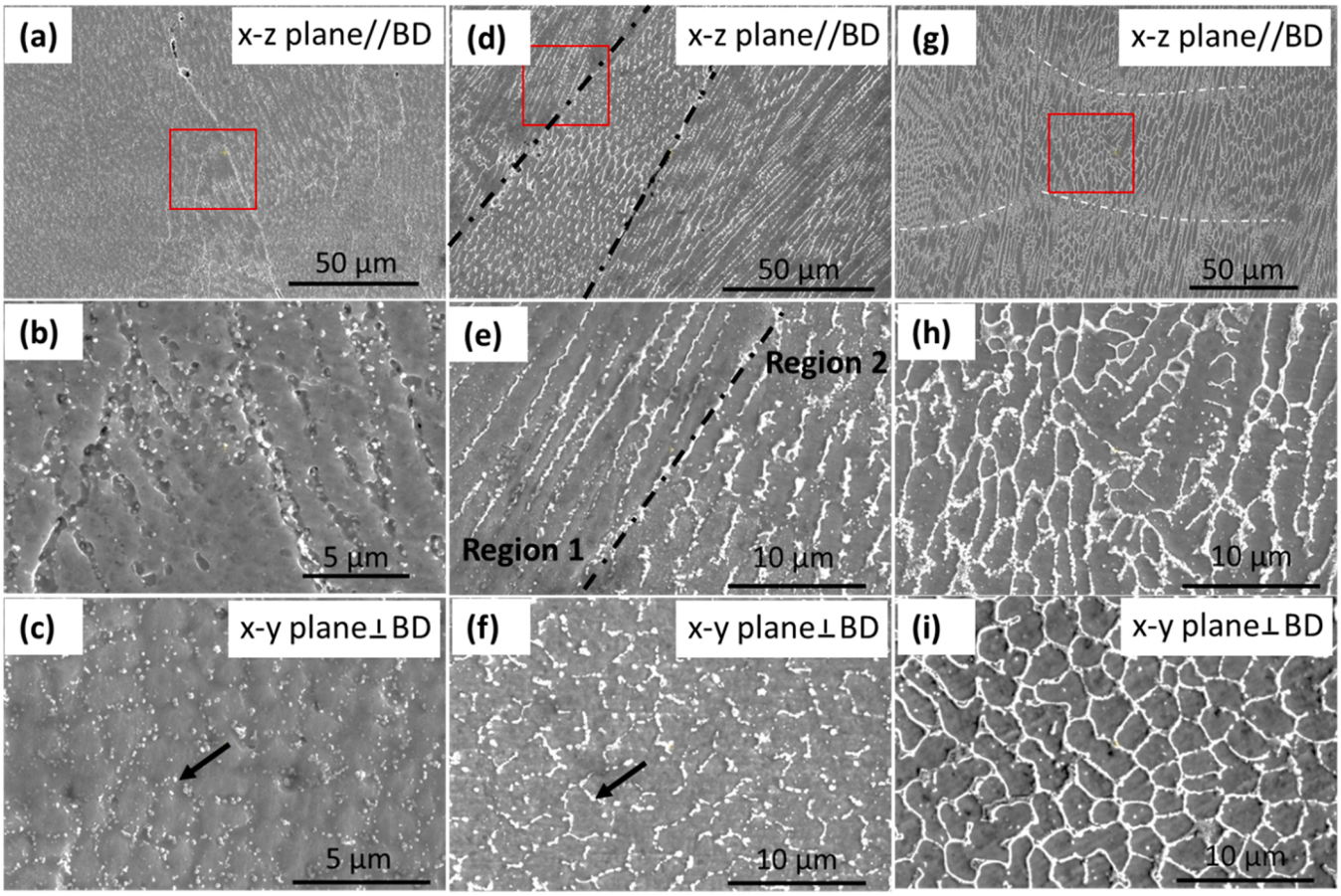

Fig. 9. SEM images of etched specimens: (a/b/c) pure-IN939; (d/e/f) IN939 + 1.5%Si; (g/h/i) IN939 + 3.0%Si.

precipitates in region 1 are long narrow strips along the boundary of primary dendrites, while in region 2, precipitates form white clusters or short laves. In Fig. 9(f), more precipitates are observed at the boundary of cellular structures, as indicated by the black arrow. This fine cellular-dendritic solidification structure is more evident in the etched IN939 + 3.0%Si specimen. Melt pools are clear and indicated by the white dashed lines in Fig. 9(g), and consist of fine sub-micro cellular structures at regions close to the melt pool border and coarse cellular structures with a size of 2–4 μm, as shown in Fig. 9(h/i).

Fig. 10 shows the SEM-EDS maps of the etched surfaces shown in Fig. 9(b/e/h). In all three specimens, the precipitates are depleted in Cr, Co, Al, and C. For the as-printed pure-IN939 specimen, the most obvious compositional enrichment for the precipitates, is Ti, while for the IN939 + 1.5%Si and IN939 + 3.0%Si specimens, strong enrichment in Si, Nb, and Ti is detected.

3.3. Mechanical properties

Results of instrumented nanoindentation hardness testing are plotted in Fig. 11(a), with error bars stemming from repeat measurements. The measured hardness H of three as-printed specimens shows a clear indentation size effect, i.e., indentation hardness increases with decreasing indentation depth h. Fig. 11(b) plots H^2 vs. $1/h$, and a linear fit is achieved at $1/h$ values below 2 μm^{-1}, consistent with the well-documented Nix-Gao model [28]. It is also notable that the indentation hardness shows a modest increase with increasing Si addition. For example, at an indentation depth of ~200 nm, the hardness increases from ~5.9 GPa for the pure-IN939 specimen to ~6.4 GPa for the IN939 + 3%Si specimen.

Mesoscale tensile tests in-situ an SEM were conducted on flat dogbone-shaped specimens with the specimen longitudinal direction (loading direction) parallel to BD. Fig. 12(a) displays the tensile test set-up with a mesoscale IN939 + 3.0%Si dog bone held by an inversed-shaped Si grip. The tensile dog-bone specimens for pure-IN939 and IN939 + 1.5%Si were cut from crack-free regions by FIB milling. All tensile specimens have a gauge section of ~ 30 μm × 10 μm × 5 μm. The measured engineering stress–strain curves are shown in Fig. 12(b). The IN939 specimens with Si additions possess higher ultimate tensile strength (UTS) than that of pure-IN939, while their tensile ductility (as measured by the tensile strain to fracture, elongation ratio, ER) is lower than that of pure-IN939. Specifically, the IN939 + 3.0%Si dog-bone specimens exhibit UTS values of ~1200 MPa, but the lowest ER of 5~8%. With no Si addition, measured UTS values for pure-IN939 dog-bone specimens are below 1000 MPa, but the corresponding ER values are in the range of 18 ~25%, agreeing well with previous studies [11]. To further understand the relationship between the microstructure changes and the observed strengthening in micro tension after Si addition, Fig. 12(c) plots the characteristic stress as a function of the inverse square root of the average grain width, w, taken from Fig. 7. Considering that it is difficult to ascertain the yield point from the initial portions of the measured engineering stress–strain curves, the engineering stress values at the strain of 0.025 are taken as the characteristic stresses. The linear fit in Fig. 12(c) indicates that the characteristic stresse scales linearly with $w^{-1/2}$, consistent with the Hall-Petch law [29,30]. Precipitates also contribute to the change in mechanical properties with Si addition. On one hand, finely dispersed precipitates serve as localized obstacles to dislocation motion, leading to higher hardness and yield stress, as documented in detail in [31]; on the other hand, the formation and coarsening of brittle precipitates with increasing Si addition decreases tensile ductility of the specimens [11].

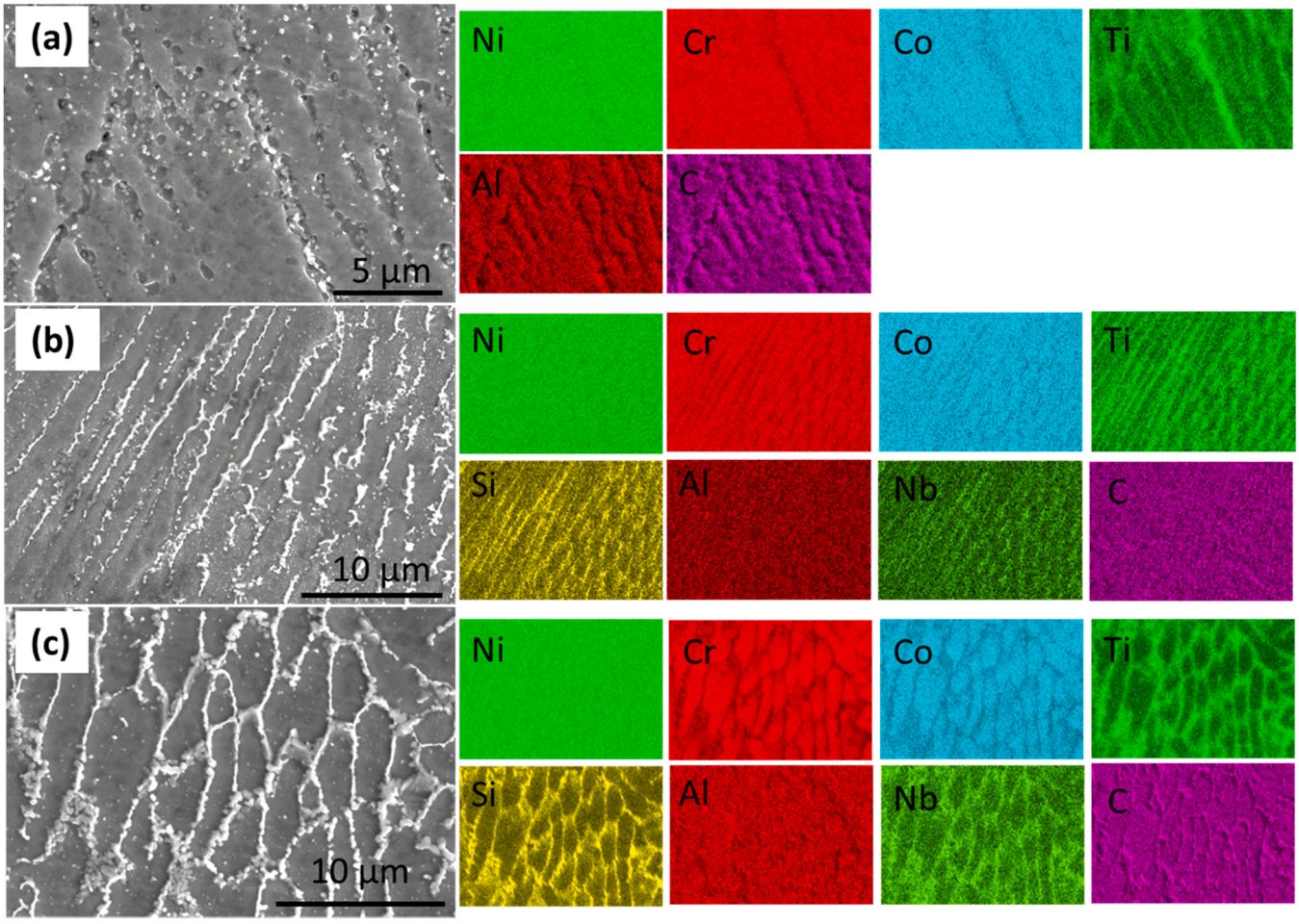

Fig. 10. EDS analysis of etched surface: (a) pure-IN939; (b) IN939 + 1.5%Si; (c) IN939 + 3.0%Si.

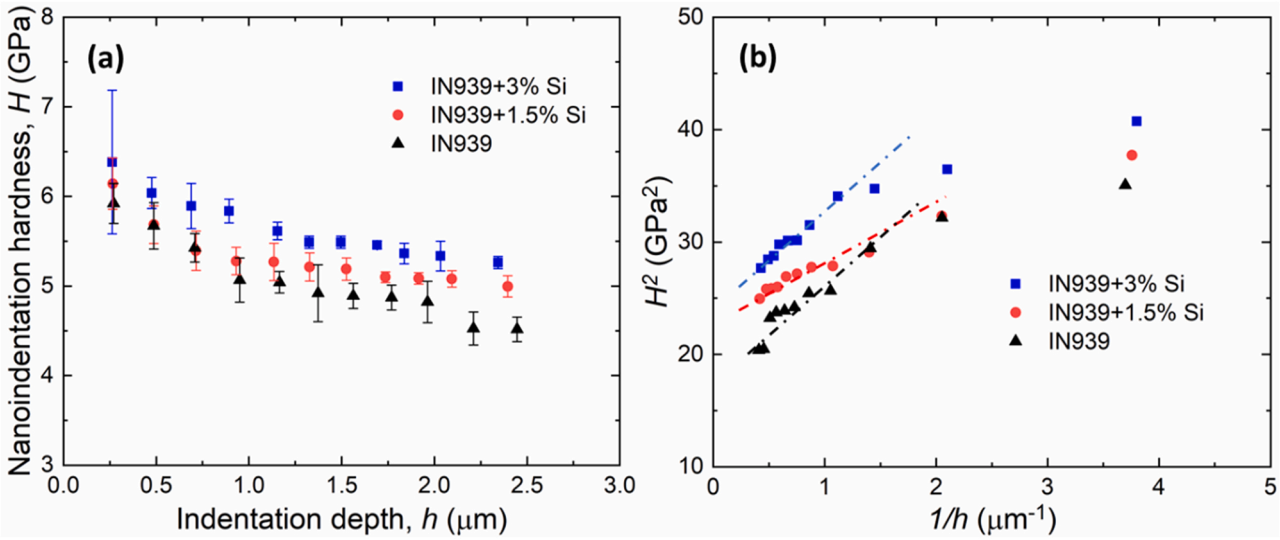

Fig. 11. Instrumented nanoindentation hardness measurements: (a) hardness H vs. indentation depth h for as-printed pure-IN939, IN939 + 1.5%Si, and IN939 + 3.0%Si; (b) plot of H^2 vs. $1/h$ for all three specimens.

Fig. 13 shows the fracture surface morphology of fractured micro tensile specimens with varying amounts of Si addition. For the pure-IN939 specimen, some degree of necking is evident and numerous slip steps can be seen on the surface of the tensile gauge section, as highlighted by the black arrow in Fig. 13(a). The density of slip steps drops noticeably with the addition of 1.5 wt% Si (Fig. 13(b)), and no obvious slip steps formed on the IN939 + 3.0%Si specimen gauge section (Fig. 13(c)). As illustrated in Fig. 13(a), the pure-IN939 specimen

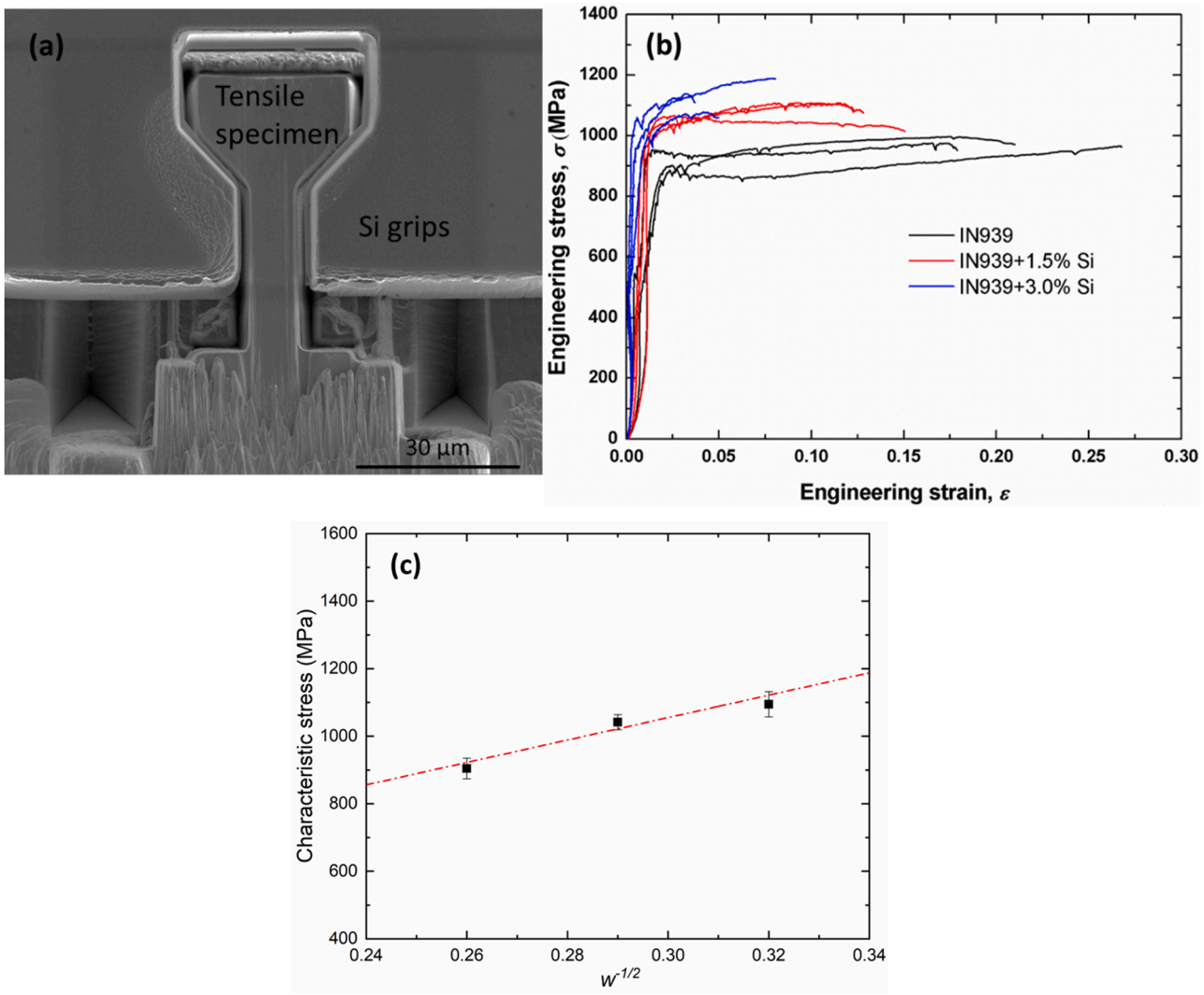

Fig. 12. (a) In situ micro tension test of a flat dogbone-shaped specimen of IN939 + 3.0%Si; (b) engineering stress-strain curves. (c) characteristics stress vs. inverse square root of average grain width.

presents a typical ductile fracture surface morphology, with microvoids and dimples visible on the fracture surface. With increasing Si addition, the fracture mode transited gradually to brittle fracture, showing flat facets on the fracture surface and little evidence of plastic deformation occurring before failure (Fig. 13(f)). These observations collectively support the conclusion that the addition of Si into IN939 results in some elevation in strength but a decrease in ductility.

4. Discussion

Contrary to other works in the literature that attempted to reduce the Si content for crack-free AM processing of unwieldable Ni-based superalloys [15–18], the present study has clearly shown that the addition of Si has significantly reduced the crack density of as-printed LPBF-AM IN939 alloy parts. These findings provide new insight into the cracking mechanisms of LPBF-AM Ni-based superalloys, as well as a different perspective on designing defect-free alloys with balanced mechanical properties. They also raise some questions that need careful analysis.

4.1. Solidification cracking of LPBF-AM IN939 alloy

It is generally agreed upon that bulk cracking observed in LPBF-AM Ni-based superalloys can be categorized into three types: solidification cracking, liquation cracking, and solid-state cracking [12]. Solidification cracking, also referred to as hot tearing, occurs in the last stage of solidification where the residual liquation in the mushy region (the front of as-solidified dendrites) distributes as thin liquid films. Cracking occurs when such thin liquid films fail to adapt to the thermal shrinkage strain, or additional liquid cannot be fed successfully from the liquid pool. Solidification cracks always form on high-angle grain boundaries and leaves two irregular and noncomplementary crack surfaces [14]. These characteristic features make solidification cracks easy to identify by fractography examination. Fig. 14 presents the solidification cracks observed in the x-y plane of the pure-IN939 specimen, perpendicular to BD. The two facing crack surfaces are different in morphology and do not present a good match upon closing. For example, the spike shaped features on crack surfaces, highlighted by the white arrow, offer confirmation for the occurrence of thin liquid film hot tearing at the last stage of solidification.

Liquation cracking, also known as heat-affected zone (HAZ) cracking, does not reveal any dendritic morphology in the fracture surfaces. Instead, it exhibits $\gamma + \gamma'$ eutectic melting, and/or γ + MC carbide eutectic melting [32]. Liquation cracking is frequently detected in welded IN939 alloy parts [33], yet no definitive evidence of this type of feature is observed in the present study, consistent with the conclusion in [12]. On the other hand, Tang et al. [12] observed the formation of solid-state cracking in as-printed IN939 alloy, which is absent in the present work. Solid-state cracking, also referred to as ductility dip

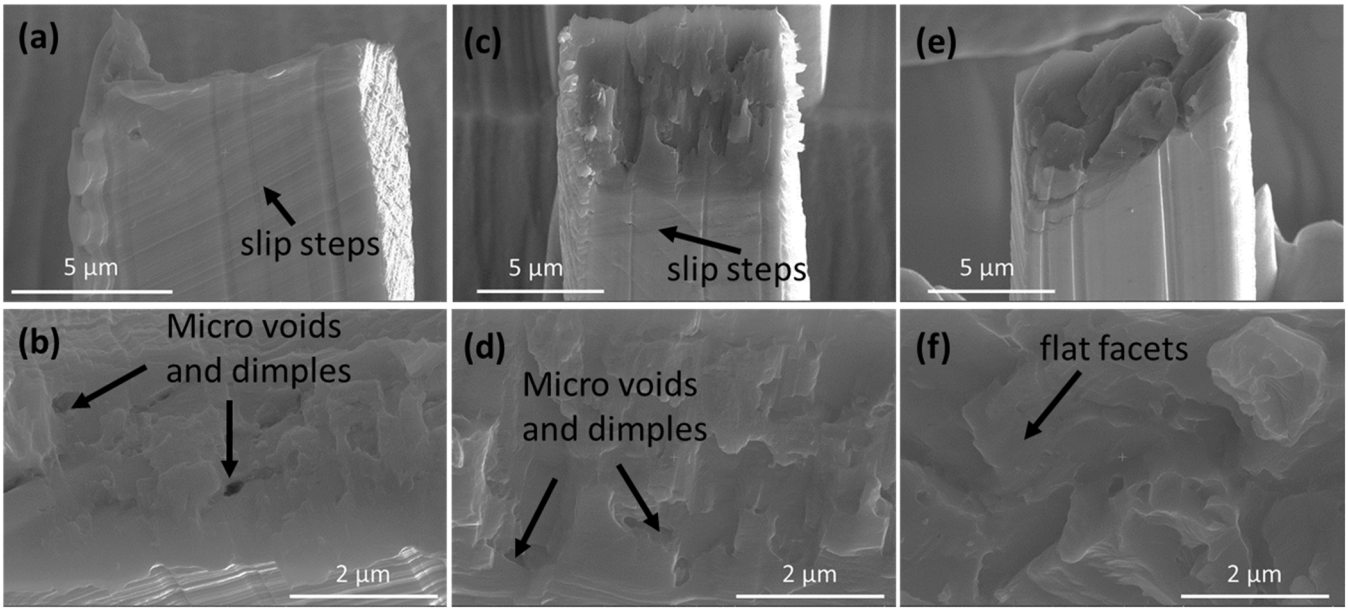

Fig. 13. Fractography of the micro tensile specimens: (a/b) pure-IN939; (c/d) IN939 + 1.5%Si; (e/f) IN939 + 3.0%Si.

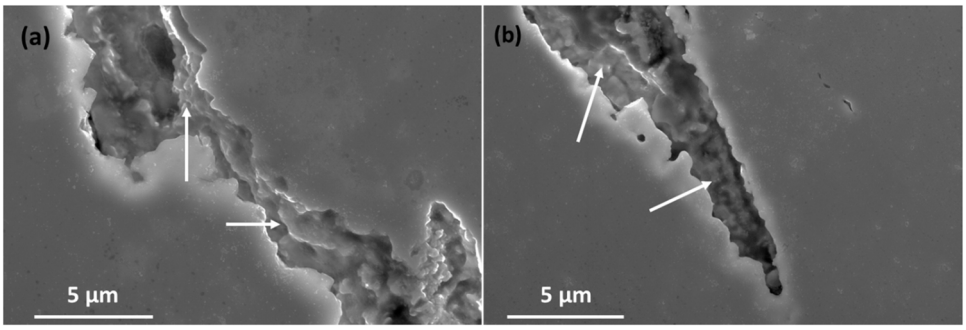

Fig. 14. SEM images of cracks in as-printed pure-IN939, showing characteristics of solidification cracking.

cracking (DDC) [34] and/or strain-age cracking (SAC) [35], involves no liquid phase and progresses entirely in the solid state. It usually occurs within a temperature range where the material's ductility drops significantly. The absence of solid-state cracking in this work can be rationalized by the micro tensile testing results. As demonstrated in Fig. 12 (b), Si addition reduces the ductility of as-printed IN939 alloy parts, and would therefore make IN939 alloy more prone to solid-state cracking if solid-state cracking were the dominant cracking mode in LPBF-AM processing. We suggest that the dominant cracking mode in LPBF-AM IN939 alloy is solidification cracking and that the solidification cracking tendency is significantly suppressed by the Si addition.

4.2. *Effect of Si addition on microstructures*

Si addition has been shown to lead to a reduction of solidification cracking in additively manufactured Al7075 alloy parts, which was attributed to the formation of new eutectic and a 90% reduction in grain size [19]. In contrast, the present study shows that Si addition to IN939 induces only moderate grain refinement. As demonstrated by data displayed in Fig. 7(d), the average columnar grain width decreased from 14.8 μm to 9.7 μm with 3 wt% Si addition, only a ~30% reduction. Moreover, the primary dendritic arm spacing (DAS) is more commonly employed when characterizing rapid solidification during LPBF-AM processing, which relates directly to the cooling rate [36,37]. Primary DAS can be measured from Fig. 9(c/f/i), and the average values are 1.7 μm, 2.8 μm, and 2.6 μm for pure-IN939, IN939 + 1.5%Si, and IN939 + 3.0%Si specimens, respectively. Primary DAS increases over 50% with 1.5 wt% Si addition and remain unchanged with more Si incorporation. This indicates the cooling rate dropped substantially with Si addition, consistent with the observation shown in Fig. 9 that more precipitates formed in IN939 + 1.5%Si and IN939 + 3.0%Si specimens, as the solidification of the precipitates would act to retard the overall solidification process.

TEM characterization was conducted to better understand the elemental distribution and crystal structure of the precipitates. Fig. 15 (a) displays the high-angle annular dark field (HAADF) STEM image and STEM-EDS maps obtained from the IN939 + 1.5%Si specimen within the area outlined by the black dashed rectangle. At least three kinds of precipitates can be identified: 1) precipitates showing enrichment in Si, Ti, Nb (Si-rich), depletion in Cr, Al, and O, and slight depletion in Co and C as indicated by white arrows. Weak depletion in Mn and Fe was also detected though their content is small and not listed in Table 1; 2) precipitates that show strong enrichment in Ti and C, as indicated by the white circles. They are likely to be Ti-rich MC type carbide; 3) precipitates that exhibit strong enrichment in Al and O, as indicated by the red circles. These are likely aluminum oxide. It is evident that most of the precipitates are the Si-rich type. The same conclusions can be drawn from the STEM-EDS maps of the IN939 + 3.0%Si specimen within the area outlined by the black dashed rectangle in Fig. 15(b), with increasing amounts of each type of precipitates due to the higher Si content.

It should be noted that in both specimens shown in Fig. 15,

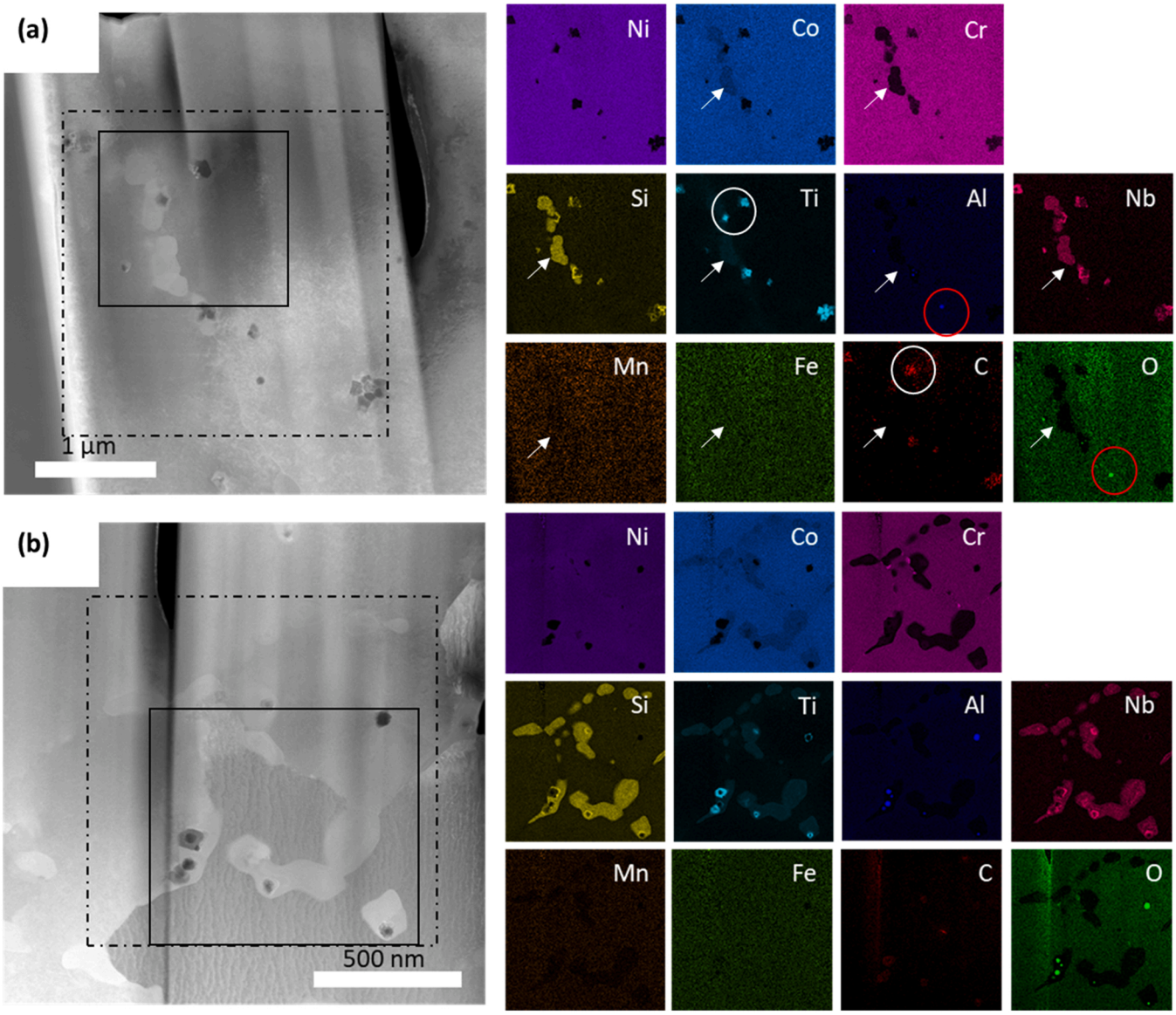

Fig. 15. STEM-EDS maps revealing the elemental distribution in precipitates of: (a) IN939 + 1.5%Si; (b) IN939 + 3.0%Si.

precipitates with simultaneous Ti and Al enrichment are not observed, suggesting that the formation of γ′ phase was suppressed due to the high effective cooling rate. Fig. 16 shows two TEM images and accompanying selective area diffraction patterns (SADPs) obtained from within the specimen area outlined by the black solid rectangles in Fig. 15. Fig. 16(a) presents the TEM image of the IN939 + 1.5%Si specimen area and five SADPs taken from within. Specifically, SADP #1 was taken from the γ matrix region within circle #1 with the specimen oriented such that the beam direction is close to a specimen < 110 > zone axis. The absence of superlattice reflections indicates the absence of the γ′ phase [7,11]. The other four SADPs were taken at the same specimen orientation, but from different precipitate types: SADPs #2 and #3 were from precipitate type 1 with enrichment in Si, Ti, and Nb, while SADPs #4 and #5 were from MC type carbides. All these SADPs are complex and unindexable from one diffraction pattern, suggestive of the complex crystal structures of the corresponding precipitates. It should be mentioned that the blurred concentric halos in SADP #2 is suggestive of the existence of some amorphous regions in the Si, Ti, and Nb rich precipitates. The analogous TEM image and five SADPs from the IN939 + 3.0%Si specimen are displayed in Fig. 16(b). With increasing Si addition, the Si, Ti, and Nb rich precipitates become less crystalline, as evidenced in SADPs #2-#5.

4.3. Further rationalization of crack susceptibility reduction with Si addition

Solidification cracking in casting and welding has been extensively studied and numerous models have been proposed [38,39]. Recently, Kou proposed a new criterion for solidification cracking, focusing on tensile deformation normal to columnar dendritic grains, lateral growth of grain towards each other, and shrinkage feeding parallel to them [40]. An index of crack susceptibility is given as:

$$\mathrm{ICS} = \left|dT/df_s^{1/2}\right| \quad near\, f_s^{1/2} = 1 \tag{2}$$

where T is temperature and f_S is the solid fraction in the semisolid. A higher ICS value suggests a higher crack susceptibility.

The solidification path of IN939 alloys with varying Si content during solidification can be calculated using Thermo-Calc and the TCNI8: Ni-Alloys database. The Scheil solidification model was selected, neglecting solid-state diffusion. Fig. 17(a/b/c) plot the calculated T vs. f_S curves for pure-IN939, IN939 + 1.5%Si, and IN939 + 3.0%Si, respectively. The change in color of each T vs. f_S curve indicates phase transformations. Fig. 17(d) displays the curve of f_S vs. $\left|dT/df_s^{1/2}\right|$ over the

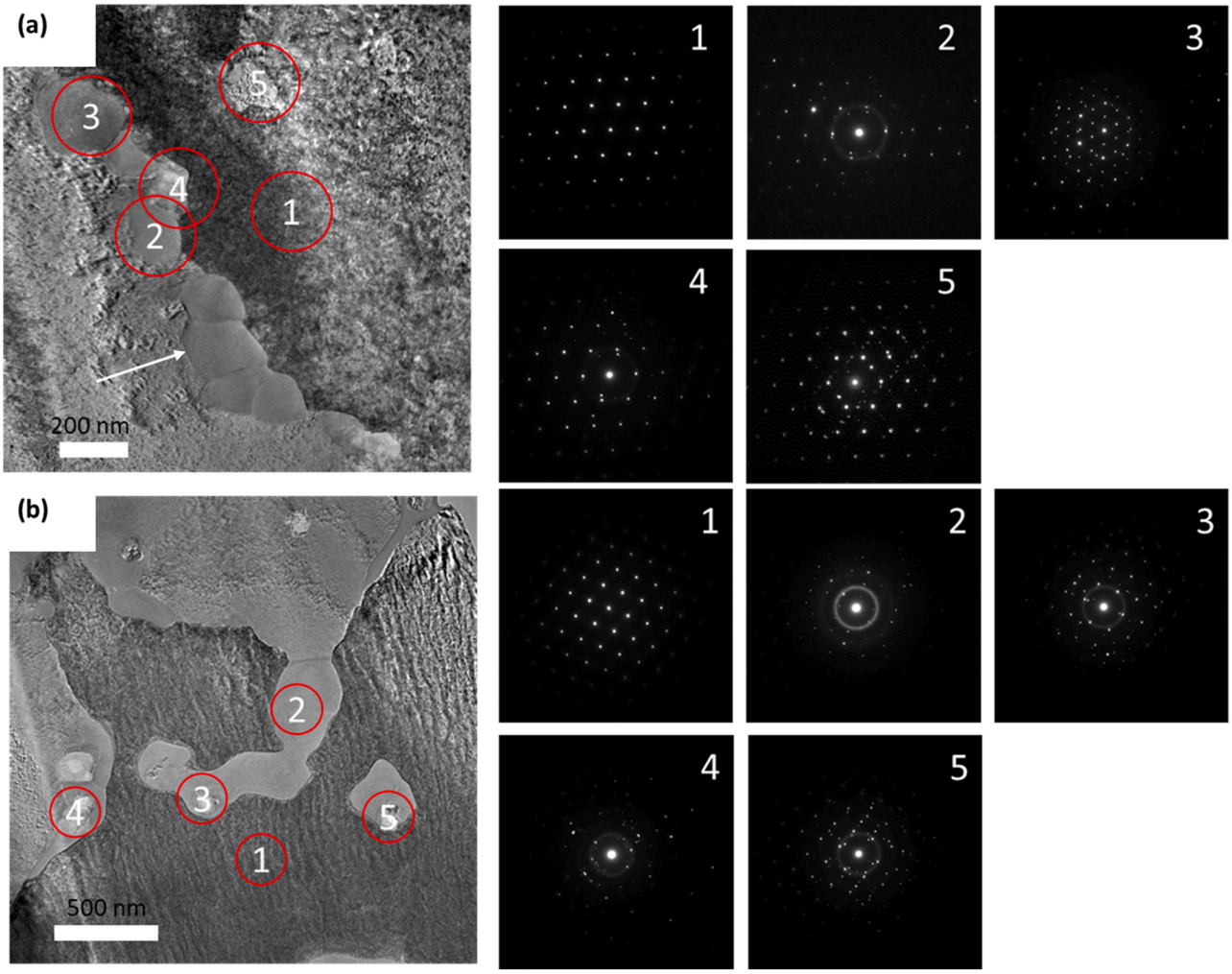

Fig. 16. Selected area diffraction patterns taken with electron beam parallel to < 110 > of the γ matrix: (a) IN939 + 1.5%Si; (b) IN939 + 3.0%Si.

range of $0.81 < f_S < 0.98$ ($0.9 < f_s^{1/2} < 0.99$). The discontinuities in the curve stem from phase transformations. The $\left|dT/df_s^{1/2}\right|$ value is higher with increasing Si content in IN939 alloy in the range of $0.81 < f_S < 0.92$ ($0.9 < f_s^{1/2} < 0.96$). However, the trend is reversed in the final stage of solidification with $f_S > 0.93$ ($f_s^{1/2} > 0.96$), i.e., IN939 alloys with Si addition exhibit lower $\left|dT/df_s^{1/2}\right|$ values, agreeing with the present experimental results that the Si addition substantially reduces solidification cracking in LPBF-AM IN939 alloy parts.

4.4. Alloy design approach for additive manufacturing

Consistency between Clyne's model [22] and Kou's model [40] in the rationalization of crack susceptibility reduction with Si addition into pure IN939 makes it necessary to discuss briefly the similarities and differences between these two models. Clyne's model considers $0.40 < f_S < 0.99$, and assumes stress relief through mass and liquid feeding in $0.40 < f_S < 0.90$ and grain separation in $0.90 < f_S < 0.99$. The ratio t_V/t_R was taken to be related to the crack susceptibility, where t_V is the vulnerable period in $0.90 < f_S < 0.99$ and t_R is the time available for stress relief in $0.40 < f_S < 0.90$. Therefore, Clyne's model is sensitive to the final stages of solidification which is critical for cracking. While Kou's model predicts the crack susceptibility by the steepness of the T vs. $(f_S)^{1/2}$ curve, it should be noted that the present selection of f_S values for ICS comparison is consistent with the "grain separation" range in Clyne's model. The present results suggest that both models are predictive in designing crack-free superalloys for additive manufacturing. The curve of T vs. f_S can be calculated using commercially available software packages and databases, making it easier to search out compositions with reduced CSC and ICS values. This alloy design approach can be applied to other elements in Ni-based superalloys as well as non-Ni-based alloy systems.

Though the observed crack reduction with Si addition agrees with both Clyne's model and Kou's model, suggesting Si addition can increase the fluidity of Ni-based alloys and accelerate the feeding behavior at the end of solidification, direct experimental evidence for such remains in need. Contributions of other factors including grain boundary angles, and grain size should also be considered. Moreover, future work is needed to ascertain the optimized Si addition content into IN939 to achieve LPBF-AM processed parts with desired mechanical properties, especially high-temperature performance. The effect of aging heat treatment on the LPBF-AM processed Ni-based alloys with Si addition is also worthy of attention. Our ongoing study indicates that the IN939 + 1.5%Si and IN939 + 3.0%Si specimens remain crack-free after the typical heat treatment procedure for Ni-based superalloys which comprises a solution annealing for 4 h at 1160 ℃ followed by a single stage aging for 16 h at 850 ℃ [11]. The mechanical properties also change significantly after aging. These results will be rerported separately.

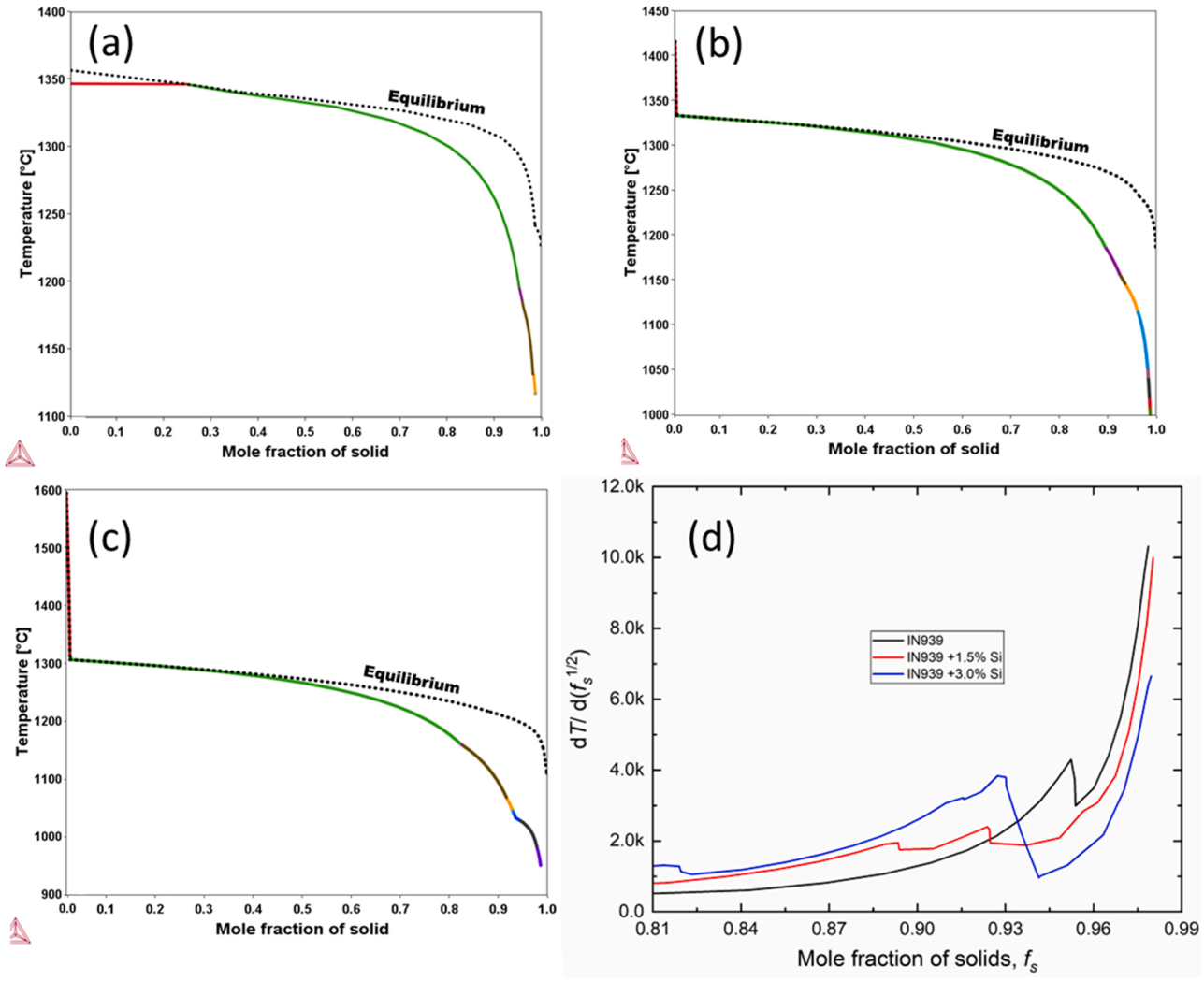

Fig. 17. (a/b/c) Calculated T vs. f_S curves for pure-IN939, IN939 + 1.5%Si and IN939 + 3.0%Si, respectively. (d) Prediction of crack susceptibility of IN939 alloys based on the steepness of T- $f_s^{1/2}$ curves in the f_s range of 0.81–0.98.

5. Conclusion

This work focuses on the fabrication of crack-free "unweldable" Ni-based superalloy parts by LPBF-AM processing and shows that minor Si addition can substantially lower the crack density in LPBF-AM IN939 alloy parts. The following conclusions are drawn:

1. Pure IN939 specimen contains numerous solidification cracks along the build direction. The addition of 1.5 wt% and 3.0 wt% Si into IN939 can substantially reduce the crack density and achieve essentially crack-free LPBF-AM IN939 alloy parts.
2. Si addition into IN939 causes changes in crystallographic orientation and average columnar grain width. The primary dendritic arm spacing increases over 50% with 1.5 wt% Si addition, indicating a substantial drop in the cooling rate due to Si addition. Si addition also results in a remarkable increase in the number of precipitates, most of which are rich in Ti, Si, and Nb. The amount, size, and distribution of precipitates affect the mechanical properties, leading to higher tensile strength and indentation hardness but lower tensile ductility.
3. Our work suggests that solidification cracking is the dominant cracking mode in LPBF-AM IN939 alloy parts. No γ′ phase is observed in as-printed specimens with or without Si addition.
4. The suppression of solidification cracking by Si addition can be qualitatively rationalized using Clyne's model and Kou's model. The calculation process of CSC and ICS indicates both models are sensitive to solidification cracking and are predictive in designing defect-free LPBF-AM Ni-based superalloys with balanced mechanical properties. This approach can be applied to other alloy systems.

Further investigations remain to be performed to fully understand the mechanism of crack reduction after the addition of Si, and to optimize the Si addition content to achieve the desired mechanical properties, especially on the high-temperature performance of LPBF-AM IN939 alloy parts.

CRediT authorship contribution statement

Bin Zhang: Conceptualization, Methodology, Investigation, Writing – original draft; **Huan Ding**: Conceptualization, Methodology, Investigation, Writing – original draft. **Andrew C. Meng**: Investigation, Writing – review & editing. **Saber Nemati**: Investigation. **Shengming Guo**: Writing – review & editing, Funding acquisition. **W.J. Meng**: Writing – review & editing, Funding acquisition.

Declaration of Competing Interest

The authors declare that they have no known competing financial interests or personal relationships that could have appeared to influence the work reported in this paper.

Data availability

Data will be made available on request.

Acknowledgement

This work was funded in part by the NSF EPSCoR program under awards OIA-2118756, OIA-1541079 and OIA-1946231, and the Louisiana Board of Regents. The use of experimental facilities at the LSU Shared Instrumentation Facility (SIF), a part of the Louisiana Core User Facilities (CUF), is acknowledged. Use of experimental facilities at the MU Electron Microscopy Core (EMC) Facilities is acknowledged.

References

[1] C. Zeng, H. Wen, B.C. Bernard, H. Ding, J.R. Raush, P.R. Gradl, M. Khonsari, S. Guo, Tensile properties of additively manufactured C-18150 copper alloys, Met. Mater. Int. 28 (2022) 168–180.
[2] H. Ding, C. Zeng, J. Raush, K. Momeni, S. Guo, Developing fused deposition modeling additive manufacturing processing strategies for aluminum alloy 7075: sample preparation and metallographic characterization, Materials 15 (2022) 1340.
[3] C. Zeng, B. Zhang, A. Hemmasian Ettefagh, H. Wen, H. Yao, W.J. Meng, S. Guo, Mechanical, thermal, and corrosion properties of Cu-10Sn alloy prepared by laser-powder-bed-fusion additive manufacturing, Addit. Manuf. 35 (2020), 101411, https://doi.org/10.1016/j.addma.2020.101411.
[4] P.D. Nezhadfar, E. Burford, K. Anderson-Wedge, B. Zhang, S. Shao, S.R. Daniewicz, N. Shamsaei, Fatigue crack growth behavior of additively manufactured 17-4 PH stainless steel: Effects of build orientation and microstructure, Int. J. Fatigue 123 (2019) 168–179, https://doi.org/10.1016/j.ijfatigue.2019.02.015.
[5] R. Arunachalam, M.A. Mannan, Machinability of nickel-based high temperature alloys, Mach. Sci. Technol. 4 (2000) 127–168.
[6] S. Sanchez, P. Smith, Z. Xu, G. Gaspard, C.J. Hyde, W.W. Wits, I.A. Ashcroft, H. Chen, A.T. Clare, Powder bed fusion of nickel-based superalloys: a review, Int. J. Mach. Tools Manuf. (2021), 103729.
[7] X. Wang, L.N. Carter, B. Pang, M.M. Attallah, M.H. Loretto, Microstructure and yield strength of SLM-fabricated CM247LC Ni-Superalloy, Acta Mater. 128 (2017) 87–95, https://doi.org/10.1016/j.actamat.2017.02.007.
[8] G. Marchese, S. Parizia, A. Saboori, D. Manfredi, M. Lombardi, P. Fino, D. Ugues, S. Biamino, The influence of the process parameters on the densification and microstructure development of laser powder bed fused inconel 939, Metals 10 (2020) 882.
[9] M.B. Henderson, D. Arrell, R. Larsson, M. Heobel, G. Marchant, Nickel based superalloy welding practices for industrial gas turbine applications, Sci. Technol. Weld. Join. 9 (2004) 13–21.
[10] M.A. González, D.I. Martínez, A. Pérez, H. Guajardo, A. Garza, Microstructural response to heat affected zone cracking of prewelding heat-treated Inconel 939 superalloy, Mater. Charact. 62 (2011) 1116–1123.
[11] P. Kanagarajah, F. Brenne, T. Niendorf, H.J. Maier, Inconel 939 processed by selective laser melting: Effect of microstructure and temperature on the mechanical properties under static and cyclic loading, Mater. Sci. Eng. A. 588 (2013) 188–195.
[12] Y.T. Tang, C. Panwisawas, J.N. Ghoussoub, Y. Gong, J.W.G. Clark, A.A.N. Németh, D.G. McCartney, R.C. Reed, Alloys-by-design: application to new superalloys for additive manufacturing, Acta Mater. 202 (2021) 417–436, https://doi.org/10.1016/j.actamat.2020.09.023.
[13] M. Sistaninia, A.B. Phillion, J.-M. Drezet, M. Rappaz, Three-dimensional granular model of semi-solid metallic alloys undergoing solidification: Fluid flow and localization of feeding, Acta Mater. 60 (2012) 3902–3911, https://doi.org/10.1016/j.actamat.2012.03.036.
[14] I. Farup, J.-M. Drezet, M. Rappaz, In situ observation of hot tearing formation in succinonitrile-acetone, Acta Mater. 49 (2001) 1261–1269, https://doi.org/10.1016/S1359-6454(01)00013-1.
[15] D. Tomus, T. Jarvis, X. Wu, J. Mei, P. Rometsch, E. Herny, J.-F. Rideau, S. Vaillant, Controlling the microstructure of Hastelloy-X components manufactured by Selective Laser Melting, Phys. Procedia 41 (2013) 823–827.
[16] R. Engeli, T. Etter, S. Hövel, K. Wegener, Processability of different IN738LC powder batches by selective laser melting, J. Mater. Process. Technol. 229 (2016) 484–491, https://doi.org/10.1016/j.jmatprotec.2015.09.046.
[17] M. Cloots, P.J. Uggowitzer, K. Wegener, Investigations on the microstructure and crack formation of IN738LC samples processed by selective laser melting using Gaussian and doughnut profiles, Mater. Des. 89 (2016) 770–784, https://doi.org/10.1016/j.matdes.2015.10.027.
[18] A. Hariharan, L. Lu, J. Risse, A. Kostka, B. Gault, E.A. Jägle, D. Raabe, Misorientation-dependent solute enrichment at interfaces and its contribution to defect formation mechanisms during laser additive manufacturing of superalloys, Phys. Rev. Mater. 3 (2019), 123602.
[19] M.L. Montero-Sistiaga, R. Mertens, B. Vrancken, X. Wang, B. Van Hooreweder, J.-P. Kruth, J. Van Humbeeck, Changing the alloy composition of Al7075 for better processability by selective laser melting, J. Mater. Process. Technol. 238 (2016) 437–445.
[20] P. Konda Gokuldoss, S. Kolla, J. Eckert, Additive manufacturing processes: selective laser melting, electron beam melting and binder jetting—Selection guidelines, Mater. (Basel) 10 (2017) 672.
[21] N. Takata, M. Liu, H. Kodaira, A. Suzuki, M. Kobashi, Anomalous strengthening by supersaturated solid solutions of selectively laser melted Al–Si-based alloys, Addit. Manuf. 33 (2020), 101152.
[22] T.W. Clyne, The influence of composition on solidification cracking susceptibility in binary alloy systems, (1981).
[23] B. Zhang, A.C. Meng, W.J. Meng, Deviation of mechanical behavior in microforming from continuum scaling: a geometrically necessary dislocation storage perspective, Int. J. Mach. Tools Manuf. 169 (2021), 103795, https://doi.org/10.1016/j.ijmachtools.2021.103795.
[24] B. Zhang, Y. Song, G.Z. Voyiadjis, W.J. Meng, Assessing texture development and mechanical response in microscale reverse extrusion of copper, J. Mater. Res 33 (2018) 978–988.
[25] L. Thijs, K. Kempen, J.-P. Kruth, J. Van Humbeeck, Fine-structured aluminium products with controllable texture by selective laser melting of pre-alloyed AlSi10Mg powder, Acta Mater. 61 (2013) 1809–1819, https://doi.org/10.1016/j.actamat.2012.11.052.
[26] P.K. Verma, S. Warghane, U. Nichul, P. Kumar, A. Dhole, V. Hiwarkar, Effect of boron addition on microstructure, hardness and wear performance of Ti-6Al-4 V alloy manufactured by laser powder bed fusion additive manufacturing, Mater. Charact. 172 (2021), 110848.
[27] Y. He, C. Montgomery, J. Beuth, B. Webler, Melt pool geometry and microstructure of Ti6Al4V with B additions processed by selective laser melting additive manufacturing, Mater. Des. 183 (2019), 108126, https://doi.org/10.1016/j.matdes.2019.108126.
[28] G.M. Pharr, E.G. Herbert, Y. Gao, The indentation size effect: a critical examination of experimental observations and mechanistic interpretations, Annu. Rev. Mater. Res. 40 (2010) 271–292.
[29] E.O. Hall, The Deformation and Ageing of Mild Steel: III Discussion of Results, Proc. Phys. Soc. Sect. B 64 (1951) 747. ⟨http://stacks.iop.org/0370-1301/64/i=9/a=303⟩.
[30] N.J. Petch, The cleavage strength of polycrystals, J. Iron Steel Inst. 174 (1953) 25–28.
[31] A.J. Ardell, Precipitation hardening, Metall. Trans. A 16 (1985) 2131–2165, https://doi.org/10.1007/BF02670416.
[32] S. Kou, Solidification and liquation cracking issues in welding, JOM 55 (2003) 37–42, https://doi.org/10.1007/s11837-003-0137-4.
[33] H. Kazempour-Liasi, M. Tajally, H. Abdollah-Pour, Effects of filler metals on heat-affected zone cracking in IN-939 superalloy gas-tungsten-arc welds, J. Mater. Eng. Perform. 29 (2020) 1068–1079, https://doi.org/10.1007/s11665-020-04617-z.
[34] M.G. Collins, J.C. Lippold, An investigation of ductility dip cracking in nickel-based filler materials-Part I, Weld. J. 82 (2003) 288.
[35] H. Kazempour-Liasi, M. Tajally, H. Abdollah-Pour, Effects of pre- and post-weld heat treatment cycles on the liquation and strain-age cracking of IN939 superalloy, Eng. Res. Express 1 (2019) 25026, https://doi.org/10.1088/2631-8695/ab4d6c.
[36] N.J. Harrison, I. Todd, K. Mumtaz, Reduction of micro-cracking in nickel superalloys processed by Selective Laser Melting: a fundamental alloy design approach, Acta Mater. 94 (2015) 59–68, https://doi.org/10.1016/j.actamat.2015.04.035.
[37] H. Davies, The structures of rapidly quenched nickel-based superalloy ribbons produced by melt spinning, Rapid Solidif. Process. Princ. Technol. (1980) 153–164.
[38] M. Rappaz, J.-M. Drezet, M. Gremaud, A new hot-tearing criterion, Metall. Mater. Trans. A 30 (1999) 449–455.
[39] D.G. Eskin, L. Katgerman, Mechanical properties in the semi-solid state and hot tearing of aluminium alloys, Prog. Mater. Sci. 49 (2004) 629–711.
[40] S. Kou, A criterion for cracking during solidification, Acta Mater. 88 (2015) 366–374.